Magnetic Resonance Imaging 55 (2019) 60–71

Contents lists available at ScienceDirect

Magnetic Resonance Imaging

journal homepage: www.elsevier.com/locate/mri

Original contribution

Compressive sensing image recovery using dictionary learning and shape-adaptive DCT thresholding

Dong Du, Zhibin Pan*, Penghui Zhang, Yuxin Li, Weiping Ku

School of Electronic and Information Engineering, Xi'an Jiaotong University, Xi'an 710049, PR China

ARTICLE INFO

Keywords:
Compressed sensing
Image reconstruction
Sparse representation
Dictionary learning
Shape-adaptive DCT
Splitting Bregman iteration

ABSTRACT

Compressed sensing (CS) has shown to be a successful technique for image recovery. Designing an effective regularization term reflecting the image sparse prior information plays a critical role in this field. Dictionary learning (DL) strategy alleviates the drawback of fixed bases. But the structure information of the image is easy to be blurred in complex regions due to the absence of sparsity in dictionary learning. This paper proposes a novel joint dictionary learning and Shape-Adaptive DCT (SADCT) thresholding method. We first propose to exploit sparsity of image in shape-adaptive regions, which is beneficial to medical images of complex textures. In this framework, the local sparsity depicts the smoothness redundancies exploited by dictionary learning. Moreover, the sparsity is enhanced especially in detail areas by the newly introduced SADCT thresholding. The attenuated SADCT coefficients are used to reconstruct a local estimation of the signal within the adaptive-shape support. Image is represented sparser in SADCT transform domain and the details of the image information can be kept with a much larger probability. Based on split Bregman iterations, an efficient alternating minimization algorithm is developed to solve the proposed CS medical image recovery problem. The results of various experiments on MR images consistently demonstrate that the proposed algorithm efficiently recovers MR images and shows advantages over the current leading CS reconstruction approaches.

1. Introduction

Compressed sensing (CS) [1,2] reconstructs the signal perfectly through the non-linear reconstruction algorithm by using the sparse characteristics of the signal. As one of the most important applications, reconstructing image from incomplete measurements has always been a topic of great interest due to its significance in various applications. For example, it is well- known that MRI scans can cause physical damage to the patient, and the application of CS means that we can use much less radiation than traditional methods of data collection [3,4]. Since exploiting the prior knowledge of the original signal plays a substantial role in CS theory, it is necessary to utilize some constraints or prior knowledge to make up for the missing information. Various efforts have been made to look for an effective sparse constraint or realistic model. With such a sparse constraint or realistic model, CS reconstruction is formulated as a constrained optimization problem, which can be solved by various methods, such as iterative shrinkage/thresholding (IST) methods [5–7] and Bregman iterative algorithms [8,9].

Finding an optimal sparse representation of image is an active research area in compressed sensing MRI (CSMRI), since a sparser representation usually leads to lower reconstruction error [10,11]. There are many prespecified sparsifying dictionaries (basis or frame), e.g., Fourier transform, discrete cosine transform, wavelets, ridgelets [12], curvelets [13], contourlets [14] and shearlets. In spite of being simple and fast computation, the analytically designed dictionaries usually capture only one type of image features and lack adaptivity to the image local structures. Due to above shortcomings, reconstruction qualities of those dictionaries are not satisfactory. Adaptive dictionary learning [10,15–17] with the capability of better matching the contents of the images can sparsify image better since they are learnt for the particular image instances or class of images. The K-SVD [18] is a typical dictionary learning method which has been applied in CSMRI for a single image [10,19–21] and has significantly improved the reconstructed image quality than those using prespecified dictionaries [22,23]. However, the structure information of the image is easy to be blurred based on the dictionary learning method of overlapping square patches. Especially with the presence of singularities or edges, ringing artifacts arising from the Gibbs phenomenon become visible because of the lack of sparsity.

In the last decade, some research works have been made towards the development of shape-adaptive transforms. The core is to construct a framework that can be used for the analysis of arbitrarily shaped

* Corresponding author.
E-mail address: zbpan@mail.xjtu.edu.cn (Z. Pan).

https://doi.org/10.1016/j.mri.2018.09.014
Received 12 October 2017; Received in revised form 13 September 2018; Accepted 16 September 2018

image segments, where the data show some unified forms. An attractive approach, named Shape-Adaptive DCT (SADCT), is proposed by Sikora et al. [24,25]. SADCT is computed by cascaded application of one-dimensional varying-length DCT transforms first on the columns and then on the rows that constitute the considered region. Actually, the use of a transform with a shape-adaptive support involves two independent problems: shape-adaptive transform and image-adaptive shape. In this paper, SADCT transform is used to solve the first problem and the Anisotropic Local Polynomial Approximation (LPA) -Intersection of Confidence Intervals (ICI) [26–28] is used to solve the second problem. SADCT has received considerable interest from the MPEG community, eventually becoming part of the MPEG-4 standard [29,30]. Furthermore, because of the better decorrelation and energy compaction properties, SADCT has shown to provide an effective method for image denoising [31]. Although SADCT features a remarkable potential for video compression applications and gets the initial realization for image denoising, this potential has been apparently ignored in the image recovery community.

In this paper, we integrate the dictionary learning (DL) and SADCT technique into a unified framework to reconstruct MR image from highly undersampled data. The dictionary trained by K-SVD characterizes the local sparsity that depicts the smoothness redundancies. Meanwhile, LPA-ICI finds the adaptive-shape region in the image patch, and then SADCT is performed in the found region to further exploit and enhance image sparsity. The proposed method has two benefits. First, because of the better decorrelation and energy compaction properties in the adaptive support set, which is shown in some unified forms. In this way, the sparsity of complex regions is enhanced by the newly introduced SADCT. As a new regularization term, SADCT can alleviate the blurred structure information of the image resulting from the dictionary learning method of overlapping square patches. Second, the proposed CS image recovery problem is formulated in the form of minimization functional under regularization-based framework. Based on split Bregman iterations, an efficient alternating minimization algorithm is developed to solve the above underdetermined inverse problem, which can achieve a fast and stable solution. By combining dictionary learning and SADCT, the data are represented sparser than dictionary learning itself. Due to the lack of sparsity in singularities or edges, the original ringing artifacts arising from the Gibbs phenomenon caused by dictionary learning can be alleviated.

The rest of this paper is organized as follows. Section 2 reviews the previous work in CSMRI (compressed sensing MRI) and states dictionary learning and Shape-Adaptive DCT. The proposed model jointing dictionary learning and Shape-Adaptive DCT thresholding method for image recovery, which applies the split Bregman iterations method, is detailed in Section 3. Section 4 demonstrates the performance of the proposed algorithm on various experiments under a variety of sampling schemes and undersampling ratios. Conclusions and future work are presented in Section 5.

2. Background

In this section, we review the previous classical work in CSMRI (compressed sensing MRI) and state dictionary learning and SADCT. The P-pixel 2D image to be reconstructed is denoted by $x \in \mathbb{C}^P$, and $f \in \mathbb{C}^m$ represents the undersampled Fourier measurements. x and f are related as $F_u x = f$, where $F_u \in \mathbb{C}^{m \times P}$ represents the partially sampled Fourier encoding matrix.

2.1. CSMRI

CSMRI reconstructs the unknown x from the k-space measurements f. In a mathematical model, CSMRI solves the linear equations $F_u x = f$ by minimizing the l_0 quasi norm of the sparsified image Ψx, where Ψ represents a global and typically orthonormal sparsifying transform. The corresponding optimization problem is

$$\min_x \|\Psi x\|_0 \quad s.\ t. \quad F_u x = f \tag{1}$$

Eq. (1) means that we should find a sparse code x for the given f using the matrix F_u, and this problem is NP-hard. It can be solved by greedy algorithms, such as orthogonal matching pursuit (OMP) [32,33]. The CSMRI reconstruction problem always uses l_1 relaxation of the l_0 quasi norm, and accounts for the noise in the k-space measurements in the following objective function [3].

$$\min_x \|F_u x - f\|_2^2 + \lambda \|\Psi x\|_1 \tag{2}$$

Because MR images are typically non-stationary, there are not universal domains in which all parts of the images are sparse. The predefined sparsifying transforms are not able to efficiently represent a specific signal and they are lack of the adaptivity to the image local structures. Recently, in medical image reconstruction field, Ravishankar et al. [10] present a method named DLMRI, which uses adaptive dictionary to reconstruct MR image by solving the following minimization problem

$$\min_{x,D,\Gamma} \sum_l \|R_l x - D\alpha_l\|_2^2 + \nu \|F_u x - f\|_2^2 \quad s.\ t. \quad \|\alpha_{ij}\|_0 \le T_0 \ \ \forall\, l \tag{3}$$

where x denotes the reconstructed image, $\Gamma = [\alpha_1, \alpha_2, \cdots \alpha_L]$ denotes the sparse coefficient matrix of image patches, R_l represents the operator that extracts the patch from x, D stands for the adaptive dictionary, α_l denotes the redundant sparse representation of $R_l x$ over D, T_0 is a threshold of the sparsity. The regularization parameter ν balances the tradeoff between the two terms, and it is empirically chosen as $\nu = \theta/\sigma$, where σ is the standard derivation of the measurement noise and θ is a positive constant. By learning adaptive transforms from image, DLMRI has exhibited superior performance compared to those methods using fixed basis. The popular K-SVD method [18] can solve Eq. (3) effectively. However, DLMRI is a patch-based redundant sparse recovery method, which indicates that the overall image is reconstructed by averaging all the overlapped patches. Although it suppresses the artificial noise, the structure information of the image is also easy to be blurred with the square patches because of the lack of sparsity in isolated points or edges. To enhance the sparsity in complex regions and restrain the flaw in dictionary learning, we use the SADCT as a new regularization term to exploit image sparsity and preserve edges, which will be presented in Section 3.

2.2. Shape-adaptive DCT (SADCT)

In the last decade, many significant research works have been made to promote the development of shape-adaptive transforms. In this field, the main focus point is to construct a model that can be used efficiently for the analysis of arbitrarily shaped image segments, where the data always exhibit some uniform behavior. SADCT transform adaptively finds the unknown smooth and anisotropic region in an image patch, and then applies DCT transform to the found region. SADCT actually involves two independent problems: (1) the transform should adapt to the shape (i.e., a shape-adaptive transform) and (2) the shape itself must adapt to the image features (i.e., an image-adaptive shape). The first problem has found a very satisfactory solution in the SADCT transform. The SADCT transform is a cascaded application of DCT transform, and it is computed by one-dimensional varying-length DCT transform first on the columns and then on the rows of the anisotropic region. The SADCT does not require computation-expensive matrix inversions or iterative orthogonalizations. It can be interpreted as a direct generalization of the classical DCT transform. So, SADCT has a computational complexity comparable to that of the conventional separable block-DCT. Fig. 1 shows the process for realizing SADCT.

In this paper, the anisotropic Local Polynomial Approximation (LPA) -Intersection of Confidence Intervals (ICI) [26–28] is used to solve the second problem. LPA is a technique which is applied for

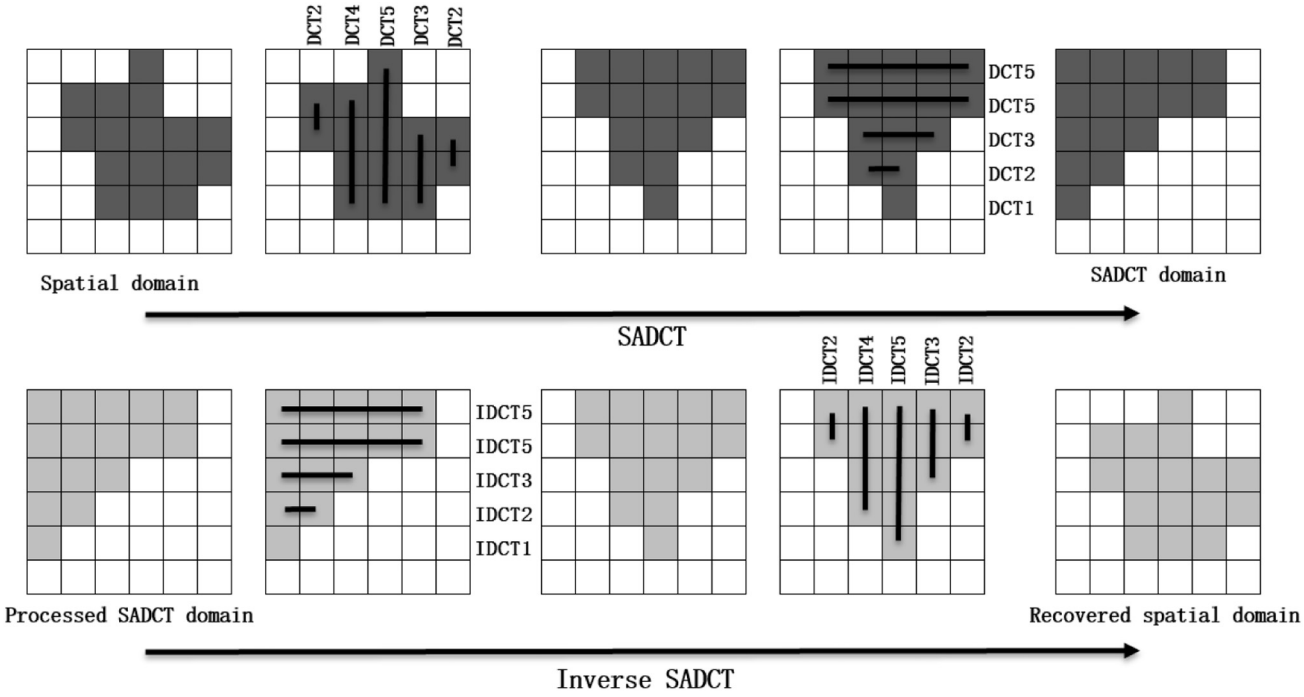

Fig. 1. Illustration of the Shape-Adaptive DCT transform and the corresponding inverse transform. Transformation is computed by cascaded application of one-dimensional varying-length DCT transforms first on the columns and then on the rows.

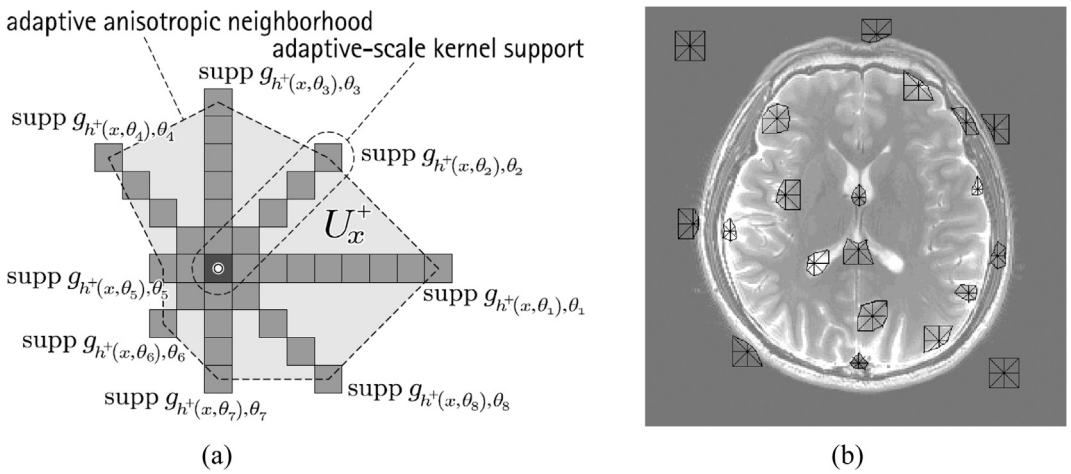

Fig. 2. Fast implementation of the LPA-ICI anisotropic neighborhoods. (a) "Linewise" one-dimensional directional LPA kernels are used for 8 directions. The anisotropic neighborhood $U_x{}^+$ is constructed as the polygonal hull of the adaptive-scale kernels' supports (left). Thus, only the adaptive scales h^+ are needed to construct the neighborhood; (b) Sketch map of the anisotropic neighborhoods $U_x{}^+$ used for SADCT of the Brain image (right). In our implementation we use $h = \{1,2,3,5,7,9\}$.

nonparametric estimation using a polynomial data fitting in a sliding window. The polynomial order m and the window function ω are crucial to the LPA. The LPA estimations are calculated by convolution against a kernel $g = w\phi\Phi^{-1}[1\ \ 0\ \ ...0]^T$, where $w = diag\ \ \omega$ is the diagonal matrix composed by the weights ω, ϕ is a vector of $m + 1$ polynomial functions $\phi_n = {}^{v^n}/_{n!}$ $n = 0, ..., m, m + 1$ and $\Phi = \phi^T w\phi$ is the Gramian matrix. Starting from a basic window function ω, one can obtain LPA's different bandwidths/scales by using scaled windows. The corresponding kernels are denoted as g_h in Fig. 2. More details about LPA can be found in Katkovnik's work [26]. The Intersection of Confidence Intervals (ICI) rule is a criterion used for the adaptive selection of the size (length/scale) of the LPA window. The purpose of ICI is to select the most appropriate one among LPA estimations by minimizing the MSE with respect to the variation of the scale. By comparing varying-scale directional kernel estimations, LPA-ICI adaptively selects a set of directional adaptive-scales for each point of the image. The length of the support (i.e., the window size) of the corresponding adaptive-scale kernels defines the shape of the transform's support in a pointwise-adaptive manner. Examples of such neighborhoods are shown in Fig. 2.

For each neighborhood SADCT is performed, the attenuated SADCT coefficients are used to reconstruct a local estimation of the signal within the adaptive-shape support. Due to the estimator is anisotropic and the shape of its support adapts to the structures existing in the patch, the support is sparser than the patch itself. By using the adaptive neighborhoods as support for the SADCT, the data are represented sparsely. In other words, if we integrate SADCT technique into the CS framework, the blocking artifacts can be suppressed and complex image features can also be preserved with larger probability for image reconstruction. The subsequent experiment results will show its

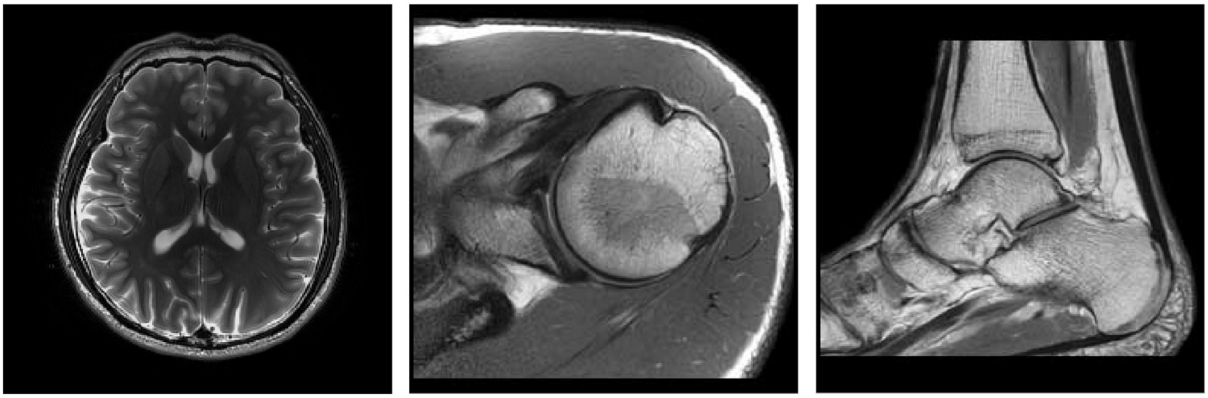

Fig. 3. Tested MR images. (a) Full-sampled Brain image; (b) Ortho1; (c) Ortho6.

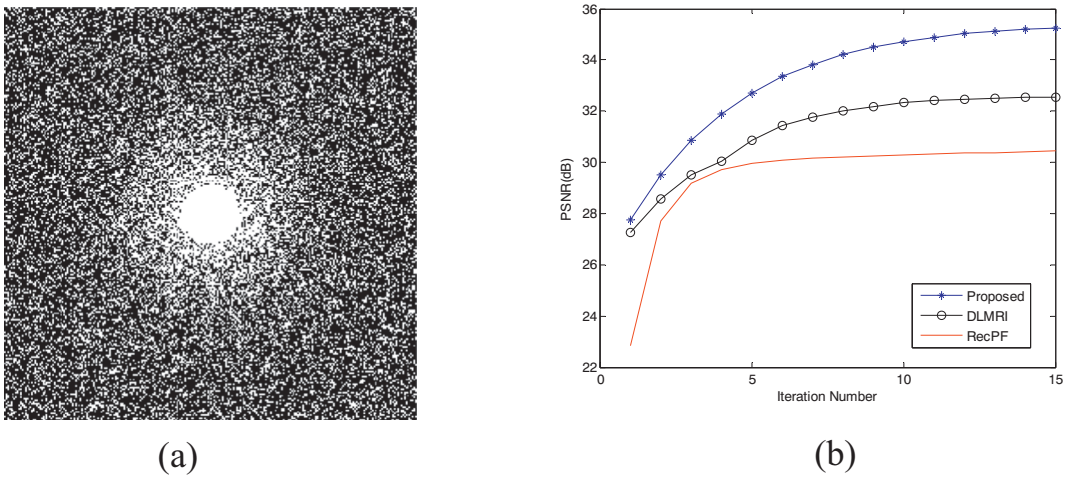

Fig. 4. (a) 2D random sampling in k-space; (b) PSNRs of DLMRI and our proposed method versus iterations for the Brain image.

effectiveness.

3. Proposed method

In this work, we propose to reconstruct the MR image by jointing adaptively learned sparsifying basis and Shape-Adaptive DCT thresholding. The split Bregman iteration is employed to solve the proposed optimization problem efficiently. The proposed method is based on the observation that the SADCT has an excellent ability to exploit image sparsity in complex region and preserves edges. Motivated by this fact, we integrate dictionary learning and SADCT technique into a unified framework to reconstruct MR image from highly undersampled data.

Yang et al. [23] present RecPF, which uses Hear wavelet basis to exploit MR image sparsity. At the same time, RecPF enhances sparsity and preserves edges by TV regularization. Adaptive dictionary learning can sparsify images better than prespecified basis due to its capability of better matching the content of the images [10]. SADCT has an excellent ability to exploit image sparsity in complex region and preserves edges better [31]. In our method, we achieve local sparsity constraint and the enhanced sparsity in edges and singularities by integrating dictionary learning and SADCT. In a mathematical expression, our proposed method can be expressed as

$$\min_{x,\alpha,D,w} \frac{1}{2}\|f - F_\mu x\|_2^2 + \lambda\|\alpha\|_0 + \tau\|\theta_w\|_1 \quad s.t. \quad x = D\alpha,\ x = w,\ w = \Omega_{SADCT}{}^{-1}(\theta_w) \tag{4}$$

where D stands for the dictionary that is learned by KSVD, and α denotes the patch-based redundant sparse representation for the whole image over D. θ_w denotes the coefficients of adaptive-shape support under SADCT and $\Omega_{SADCT-1}(\theta_\omega)$ denotes the inverse SADCT transform for θ_w. λ and τ are regularization parameters which control the trade-off among three terms in Eq. (4).

In order to solve the minimization problem of Eq. (4), an alternating SBI algorithm is applied. We finally achieve the following sub-problems

$$x^{(k+1)} = \underset{x}{\operatorname{argmin}} \frac{1}{2}\|f - F_\mu x\|_2^2 + \frac{\mu_1}{2}\|x - D^{(k)}\alpha^{(k)} - b^{(k)}\|_2^2 + \frac{\mu_2}{2}\|x - w^{(k)} - c^{(k)}\|_2^2 \tag{5}$$

$$D^{(k+1)}, \alpha^{(k+1)} = \underset{D,\alpha}{\operatorname{argmin}} \lambda\|\alpha\|_0 + \frac{\mu_1}{2}\|x^{(k+1)} - D\alpha - b^{(k)}\|_2^2 \tag{6}$$

$$w^{(k+1)} = \underset{w}{\operatorname{argmin}} \tau\|\theta_w\|_1 + \frac{\mu_2}{2}\|x^{(k+1)} - w - c^{(k)}\|_2^2 \tag{7}$$

$$b^{(k+1)} = b^{(k)} - x^{(k+1)} + D^{(k+1)}\alpha^{(k+1)} \tag{8}$$

$$c^{(k+1)} = c^{(k)} - x^{(k+1)} + w^{(k+1)} \tag{9}$$

where μ_1 and μ_2 are fixed value parameters for improving the numerical stability of the algorithm. By SBI, the minimization for Eq. (4) is transformed into three sub-problems, namely, x, α, w sub-problems. In the following, we will provide the implementation details to obtain the efficient solutions to each separated sub-problem.

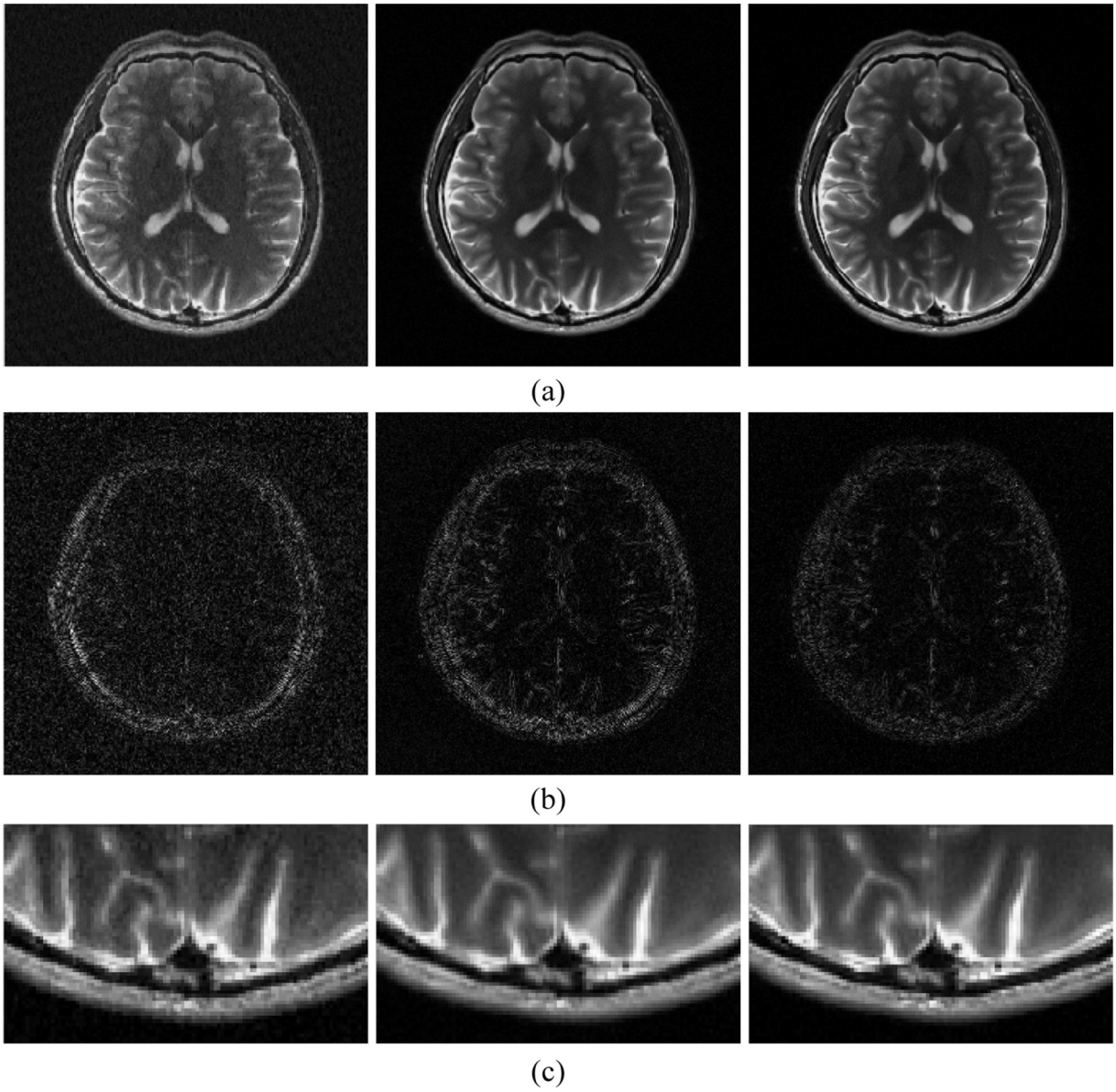

Fig. 5. Visual comparison of the Brain image reconstructions using three methods when 33% data are sampled employing 2D random sampling. (a) Reconstructed images based on RecPF, DLMRI and our proposed method, respectively; (b) The reconstruction error of magnitudes corresponding to the above reconstructions; (c) Zoomed-in regions corresponding to Fig. 5(a).

Table 1
PSNR(dB) comparisons on test image using different sampling schemes at a ratio of 33% with RecPF (top), DLMRI (middle), and our proposed method (bottom). The PSNR values of our proposed method are shown in bold.

	Sampling pattern		
Test image	2D random	1D Cartesian	Pseudo radial
Brain	30.46	29.71	30.27
	32.56	30.13	31.15
	35.25	**32.20**	**34.11**
Ortho1	32.09	30.77	30.63
	34.25	32.53	32.46
	36.06	**33.96**	**35.34**
Ortho6	31.48	30.49	30.78
	32.81	31.21	31.87
	34.90	**32.95**	**34.66**

3.1. *x* Sub-problem

When given $\alpha^{(k)}$ and $w^{(k)}$, the sub-problem of Eq. (5) consists of minimizing a strictly convex quadratic function that has an analytic solution, which satisfies the normal equation

$$(F_{\mu}^{H}F_{\mu} + (\mu_1 + \mu_2)I)x^{(k+1)} = \mu_1(D^{(k)}\alpha^{(k)} + b^{(k)}) + \mu_2(w^{(k)} + c^{(k)}) + F_u^H f \tag{10}$$

As for MR image compressed sensing recovery, it is expensive to solve Eq. (10) directly. However, we can apply a simplification by transforming from image space to Fourier space [10,19]. Let $F \in \mathbb{C}^{P\times P}$ denote the full Fourier encoding matrix that has been normalized such that $F^HF = I_P$, the superscript H denotes the Hermitian transpose operation. Fx represents the full k-space data. If the Fourier transform is applied to both sides of the Eq. (10), we can obtain Eq. (11) by using the convolution theorem for Fourier transform.

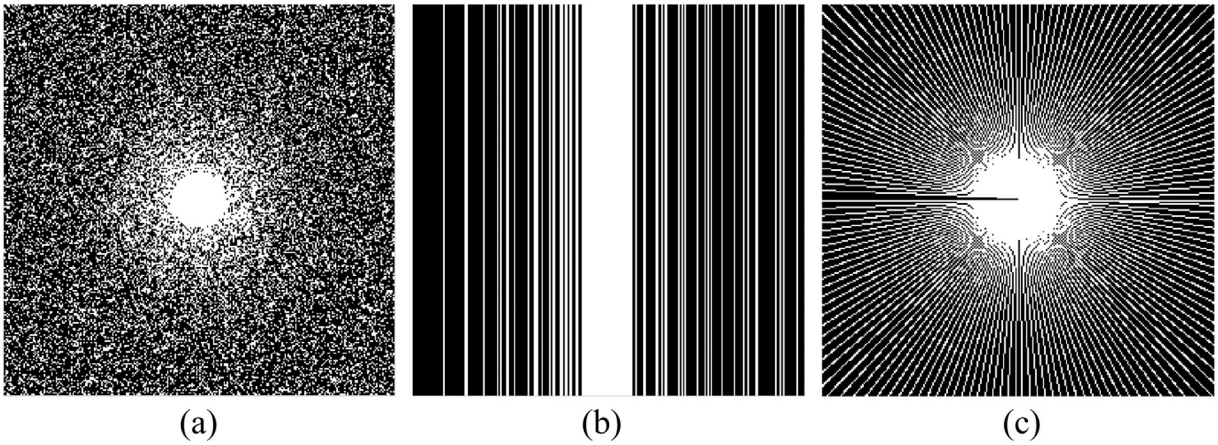

Fig. 6. Three different sampling schemes at a ratio of 33%. (a) 2D Random; (b) 1D Cartesian; (c) Pseudo radial.

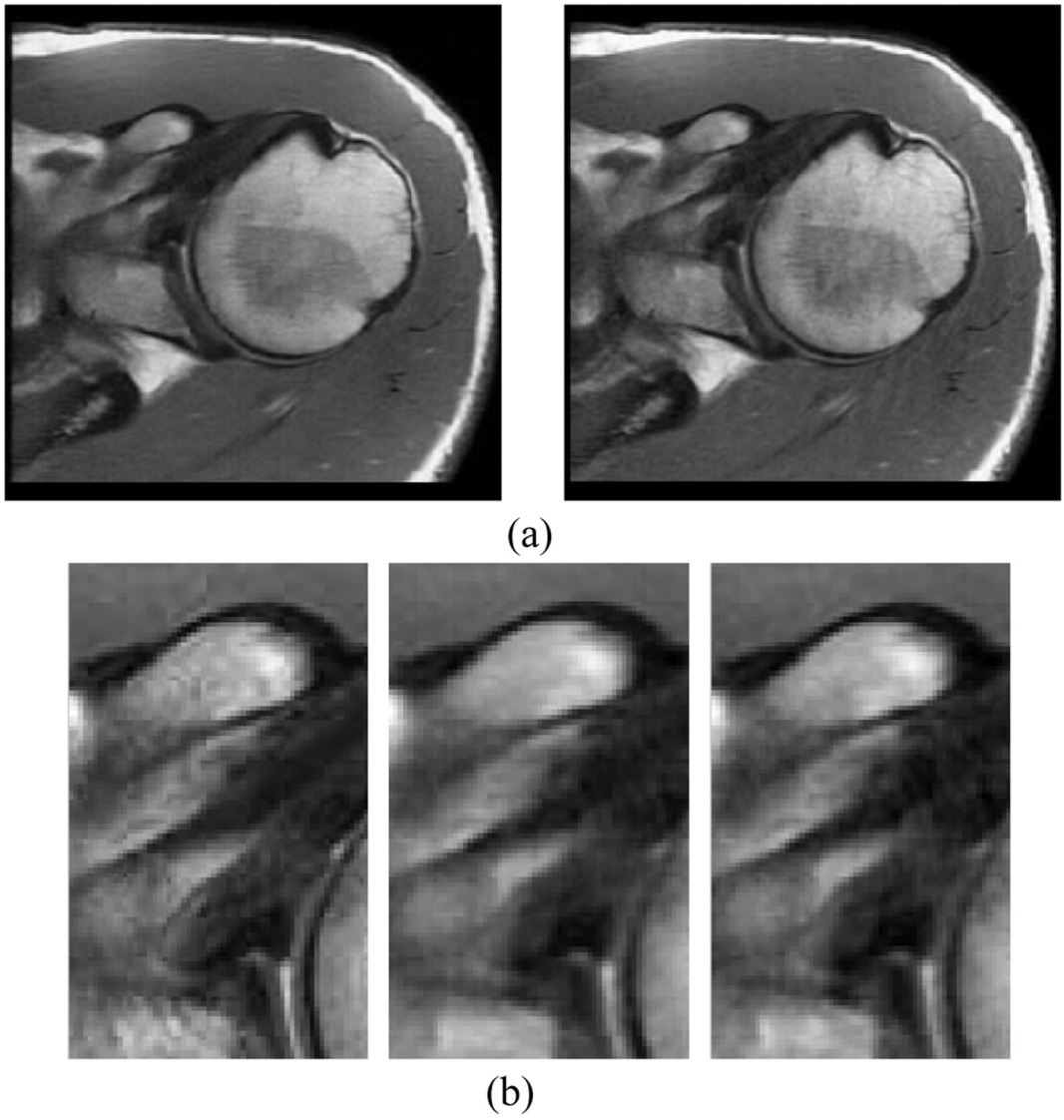

Fig. 7. Visual comparison of Ortho1 reconstructions using DLMRI and our proposed method when 33% data are sampled with the 1D Cartesian sampling scheme. (a) Reconstructed images based on DLMRI and our proposed method, respectively; (b) Zoomed-in regions: original image (left), DLMRI (middle), our proposed method (right).

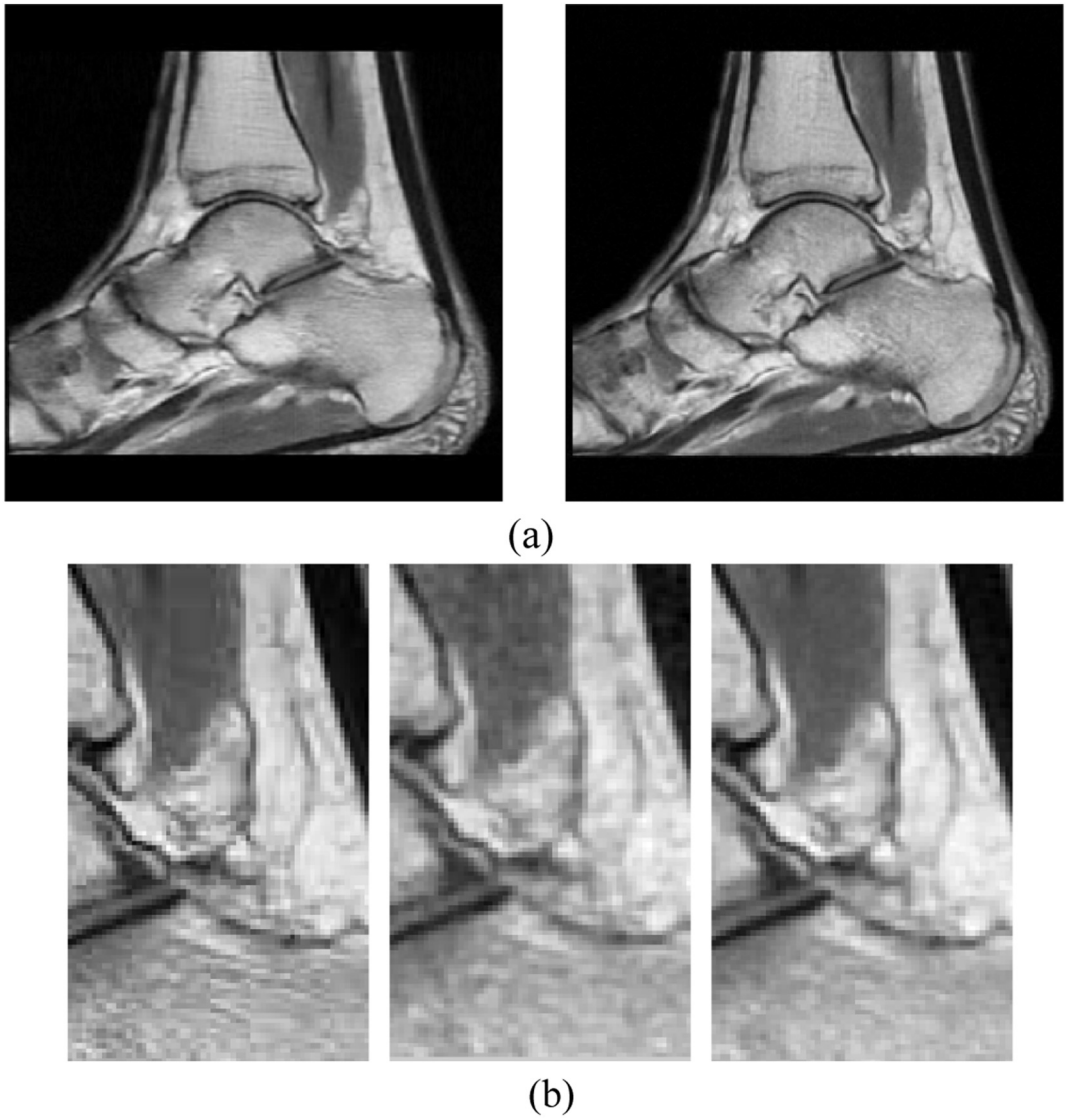

Fig. 8. Visual comparison of Ortho6 reconstructions using DLMRI and our proposed method when 33% data are sampled with the pseudo radial sampling scheme. (a) Reconstructed images based on DLMRI and our proposed method, respectively; (b) Zoomed-in regions: original image (left), DLMRI (middle), our proposed method (right).

$$(F(\mu_1+\mu_2)IF^H + FF_\mu{}^HF_\mu F^H)Fx^{(k+1)} = F(\mu_1(D^{(k)}\alpha^{(k)} + b^{(k)}) + \mu_2(w^{(k)} + c^{(k)}) + F_\mu{}^Hf) \quad (11)$$

The matrix $FF_\mu{}^HF_\mu F^H$ is a diagonal matrix consisting of ones and zeros. The ones are at those diagonal entries that correspond to sampled locations in k-space. Due to the entry in left bracket in Eq. (11) is a diagonal matrix, Eq. (5) can be solved easily by the following equation

$$x^{(k+1)} = F^{-1}\left(\frac{F(\mu_1(D^{(k)}\alpha^{(k)} + b^{(k)}) + \mu_2(w^{(k)} + c^{(k)}) + F_\mu{}^Hf)}{(F(\mu_1+\mu_2)IF^H + FF_\mu{}^HF_\mu F^H)}\right) \quad (12)$$

3.2. α Sub-problem

After having $x^{(k+1)}$ in hand, the α sub-problem is a sparse representation for image patches with respect to variable D and α. For simplicity, the subscript k is omitted in the following discussion. Viewing $r = x - b$ as some type of the noisy observation of x, the sub-problem of Eq. (6) becomes

$$\underset{D,\alpha}{\operatorname{argmin}} \frac{1}{2}\|r - D\alpha\|_2^2 + \frac{\lambda}{\mu_1}\|\alpha\|_0 \quad (13)$$

The strategy to solve Eq. (13) is to alternatively update the dictionary D and coefficient matrix α, which is the same as the method used in K-SVD and DLMRI algorithms [10,18]. In the dictionary updating step, we conduct K-SVD algorithm to train a learned dictionary using part of the patches extracted from r. While in the step of sparse coding, we solve Eq. (13) with a fixed dictionary D by the greedy matching pursuit (OMP) algorithm.

3.3. w Sub-problem

After having $x^{(k+1)}$ in hand, similar to the process in α sub-problem, the sub-problem of Eq. (7) can be written as

$$\underset{w}{\operatorname{argmin}} \frac{1}{2}\|z - w\|_2^2 + \frac{\tau}{\mu_2}\|\theta_w\|_1 \quad (14)$$

where $z = x - c$. Due to the complicated definition of θ_w, it is not easy to solve Eq. (14) directly. We view z as a type of the noisy observation w and assume all elements of $e (e = z - w, e \in \mathbb{C}^P)$ are i.i.d. (independent identically distributed) with zero-mean and variance σ^2, P equals the size of the image. Then, according to the law of large numbers, for any $\varepsilon > 0$, we have

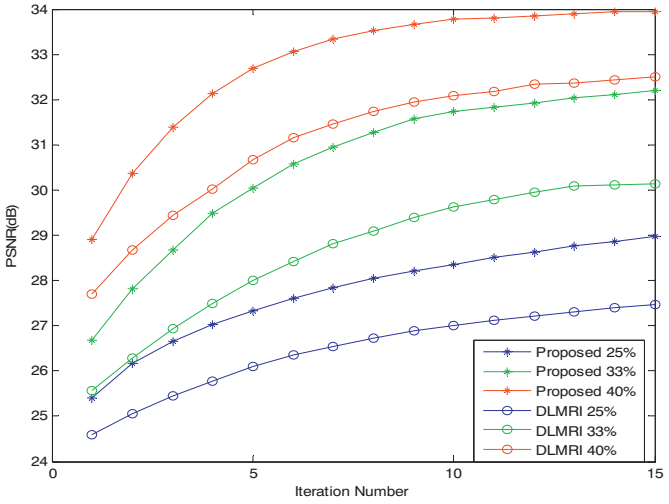

Fig. 9. PSNRs of the DLMRI and our proposed method versus iterations for the Brain image employing 1D random Cartesian sampling of k-space with different sampling ratios. The sampling ratios are 25%, 33% and 40% respectively.

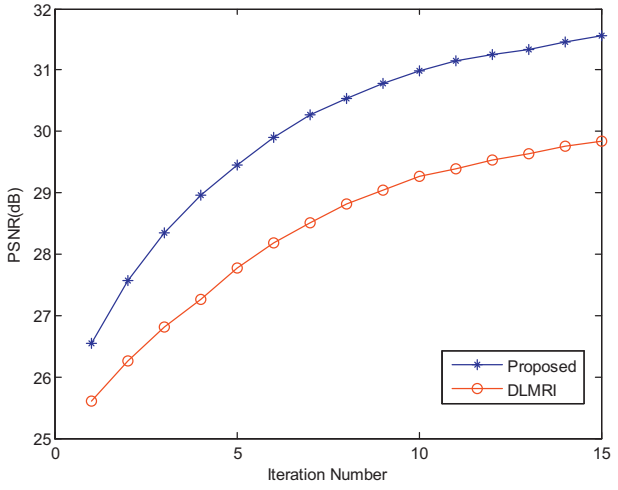

Fig. 10. PSNRs of the DLMRI and our proposed method versus iterations for the brain image employing 1D random Cartesian sampling with the Gaussian noise added in k-space.

Table 2
PSNR(dB) comparisons on test image using 2D Random sampling schemes at a ratio of 33% with different dictionary learning algorithms.

Method	Brain	Ortho1	Ortho6
KSVD	32.56	34.25	32.81
KSVD + SADCT (proposed)	35.25	36.06	34.90
MOD	31.85	33.16	31.72
MOD + SADCT	34.97	35.88	34.68
BKSVD	32.93	34.75	33.29
BKSVD + SADCT	35.61	36.35	35.31
FDLCP	35.16	36.28	35.04
FDLCP + SADCT	35.79	36.94	35.82

$$\lim_{P\to\infty} \Pr\left\{\left|\frac{1}{P}\|z-w\|_{l_2}^2-\sigma^2\right|<\frac{\varepsilon}{2}\right\}=1 \tag{15}$$

Meanwhile, θ_e ($\theta_e=\theta_z-\theta_w, \theta_e\in\mathbb{C}^{K_\theta}$) is used to denote the error vector in SADCT transform domain. K_θ equals the sum of the sizes of all adaptive-shape regions for the total image patches. In a mathematical expression, K_θ can be expressed as

$$K_\theta=\sum_{i=1}^{J} n(i) \tag{16}$$

where J denotes the number of patches, $n(i)$ denotes the size of adaptive-shape regions for the i-th image patch. Due to the orthogonal property of SADCT transform, we consider all elements of θ_e are also i.i.d. with zero-mean and variance σ^2, and we can obtain the following formula

$$\lim_{K_\theta\to\infty} \Pr\left\{\left|\frac{1}{K_\theta}\|\theta_z-\theta_w\|_{l_2}^2-\sigma^2\right|<\frac{\varepsilon}{2}\right\}=1 \tag{17}$$

By Eq. (15) and Eq. (17), we have

$$\frac{1}{P}\|z-w\|_2^2=\frac{1}{K_\theta}\|\theta_z-\theta_w\|_2^2 \tag{18}$$

Incorporating Eq. (18) into Eq. (14) leads to

$$\theta_w=\underset{\theta_w}{\operatorname{argmin}}\frac{1}{2}\|\theta_z-\theta_w\|_2^2+\frac{K_\theta\tau}{\mu_2 P}\|\theta_w\|_1 \tag{19}$$

Due to the θ_w in Eq. (19) is component-wise and has a complicated definition, each of components can be solved by a component-wise (soft) shrinkage procedure independently with K_θ. Similar to the work [36], this shrinkage can be written as

$$\theta_w=\operatorname{sign}(\theta_z)\odot\max\left\{|\theta_z|-\frac{K_\theta\tau}{u_2 P},0\right\} \tag{20}$$

where $\odot$ denotes the component-wise product, and sign, max and absolute value functions are applied in component-wise fashion. The closed-form solution of Eq. (14) can be written as

$$w=\Omega_{SADCT}^{-1}(\theta_w)=\Omega_{SADCT}^{-1}\left(\operatorname{sign}(\theta_z)\odot\max\left\{|\theta_z|-\frac{K_\theta\tau}{u_2 P},0\right\}\right) \tag{21}$$

Given the updated x, α, w, we execute Eq. (8) and Eq. (9) to obtain b and c, and then go to the next iteration.

The whole proposed algorithm can be summarized in Algorithm 2, and the algorithm is initialized with a zeros-filled Fourier reconstruction $F_\mu^H f$.

Algorithm 2. The detailed descriptions of the proposed MR image recovery framework.

Input: k-space measurements f, λ, τ, μ_1, μ_2, $k_{\max}$;

Output: Reconstructed MR image x;

Initialization: $x=x^{(0)}=F_\mu^H f$; $(b^{(0)},c^{(0)})=(0,0)$

Iteration:

For $k=0,1,2,\cdots,k_{\max}-1$

1. $r^{(k)}=x^{(k)}-b^{(k)}$; $z^{(k)}=x^{(k)}-c^{(k)}$;
2. Using Eq. (13) to compute $\alpha^{(k)}$ and $D^{(k)}$ by K-SVD algorithm;
3. For each patches of $z^{(k)}$ using LPA-ICI algorithm to learn an adaptive-shape support;
4. Apply SADCT transform to each adaptive-shape support and obtain $w^{(k)}$ using Eq. (21);
5. Compute $x^{(k+1)}$ using Eq. (12);
6. $\alpha^{(k+1)}=\alpha^{(k)}$; $w^{(k+1)}=w^{(k)}$;
7. Update $b^{(k+1)}$ and $c^{(k+1)}$ using Eq. (8) and Eq. (9);

End

Output $x^{(k+1)}$

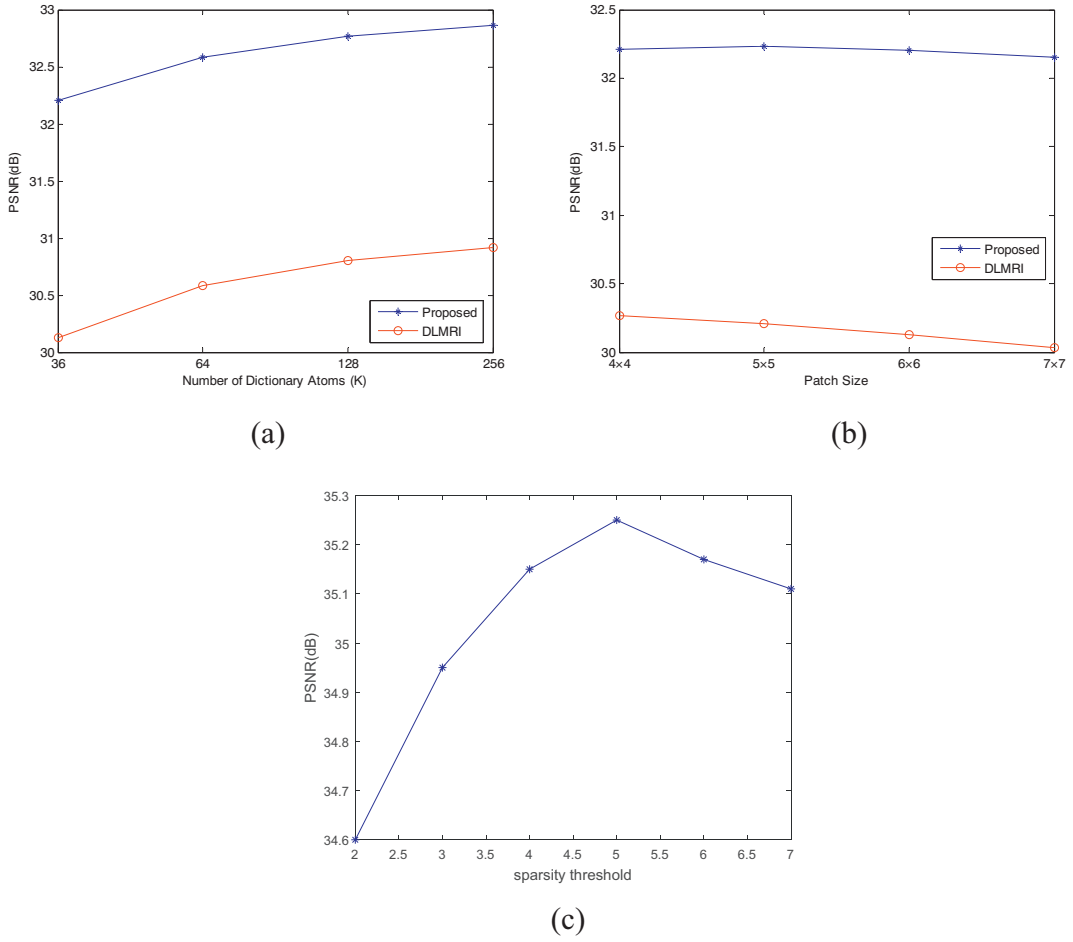

Fig. 11. Parameter evaluation. (a) PSNRs versus the number of dictionary atoms for the brain image employing 1D random Cartesian sampling; (b) PSNRs versus patch size with $K = 36$ under the same conditions with Fig. 11(a); (c) PSNRs versus sparsity threshold.

Table 3
PSNR(dB) and Time(s) comparisons on test image Brain with different patch overlap stride.

Overlap stride	$r = 1$	$r = 2$	$r = 3$	$r = 4$
PSNR (dB)	35.25	34.96	34.57	33.97
Time (s)	3346.87	1140.85	698.71	359.37

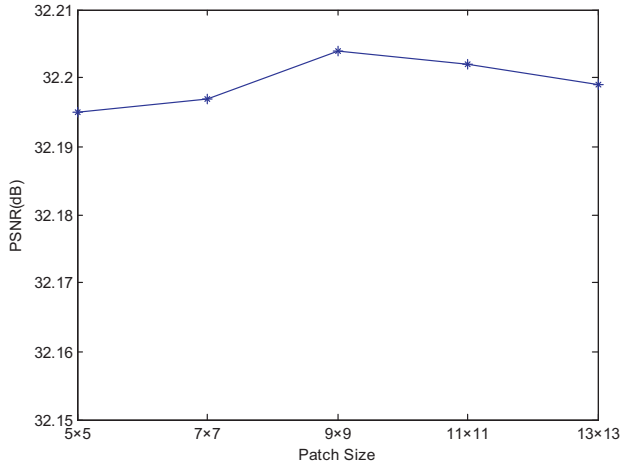

Fig. 12. Parameter evaluation. PSNRs versus patch size used in SADCT.

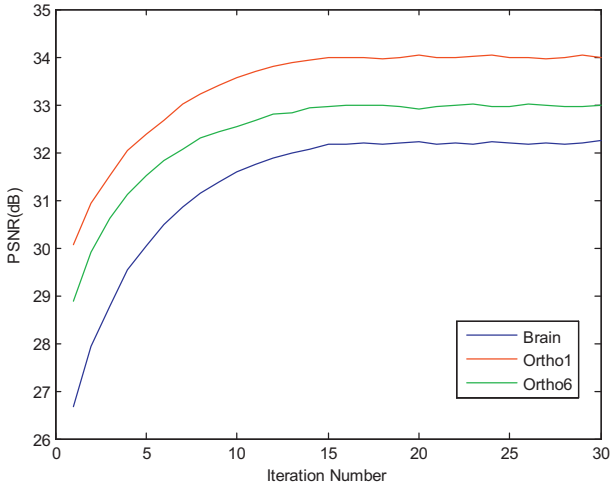

Fig. 13. PSNRs of our proposed method versus iterations for the three test images employing 1D random Cartesian sampling.

4. Experimental results

In this section, the performance of the proposed method is tested using some sampling schemes with different sampling ratios. We use the peak signal-noise ratio (PSNR) in dB to evaluate our simulation results. Similar to a lot of previous works on MR image reconstruction using compressed sensing [3,10,23], 1D random Cartesian sampling, 2D

random sampling, and pseudo radial sampling are adopted for comparison in this paper. The images used in the experiments are shown in Fig. 3. Fig. 3(a) is the T2-weighted brain image, which is acquired from a healthy volunteer at 3-T Siemens Trio Tim MRI scanners using the T2-weighted turo spin echo sequence (matrix size = 256 × 256, TR/TE = 6100/99ms, field of view = 220 × 220 mm^2, slice thickness = 3.0mm). In our experiments, we use the real-valued MR image by taking the absolute value operation to T2-weighted brain image. Fig. 3(b) and (c) are two images with a size of 256 × 256 that are contained in the algorithm package RecPF_v1.1 [38]. Our proposed method is compared with the TV + Wavelet based RecPF method and the patch-based DLMRI method. All implementations are coded in Matlab (R2012a). Computations are performed with an Intel Core i7 CPU at 3.40 GHz and 16GB memory. The Matlab implementation of RecPF [23] is available from the author's website [38], and the code of the DLMRI is available from the website [39]. For the RecPF, we tune the regularization parameters to give the best performance. The parameters for DLMRI method are set as the default values, each patch size is 6 × 6, the patch overlap is 1, a square dictionary (the number of atoms is 36) is learnt from 7200 randomly selected patches using 10 iterations, sparsity level is set as 5. The parameters for the part of dictionary learning in our proposed method follow the same setup as above, with additional choices of $k_{\max} = 15$, $\mu_1 = \mu_2 = 1.25 \times 10^{-3}$. The proposed method also applies patches with the size of 9 × 9 and the overlap of 1 for SADCT. Narrow one-dimensional "linewise" directional LPA kernels $\{g_h, \theta_k\}_{h\in\{1,2,3,4,5\}}$ are used for $K = 8$ directions.

4.1. Visual and PSNR comparisons

Figs. 4 and 5 show the performance of the RecPF, DLMRI and the proposed method on the Brain image employing 2D random sampling of k-space at a ratio of 33% respectively. The Fourier domain sampling pattern is shown in Fig. 4(a). Fig. 4(b) illustrates the convergence speed of RecPF, DLMRI and the proposed method. The proposed method can steadily yield higher PSNR than RecPF and DLMRI after 15 iterations. The PSNRs of the reconstructions using RecPF, DLMRI and the proposed method are 30.46 dB, 32.56 dB and 35.25 dB, respectively. From the recovered images and the corresponding error images, which are shown in Fig. 5(a) and (b), we can see that our method achieves much better visual quality than RecPF and DLMRI. It can be observed that the proposed method recovers not only sharp large-scale edges but also fine-scale image details. In contrast, RecPF and DLMRI still suffer from some undesirable artifacts and lost details. Such difference appears particularly in the zoomed-in regions shown in Fig. 5(c). The high PSNR performance of our method is attributed to the efficient employment of the joint dictionary learning and Shape-Adaptive DCT (SADCT) thresholding. In our proposed framework, the local sparsity that depicts the local smoothness redundancies is exploited by dictionary learning. Meanwhile, the sparsity in complex region is enhanced by the newly introduced Shape-Adaptive DCT modeling.

4.2. Sampling schemes and ratios

Table 1 shows the performance on the Brain image, Ortho1 and Ortho6 under different sampling schemes at a ratio of 33% using RecPF, DLMRI and our proposed method. All the sampling schemes (1D Cartesian, 2D random and pseudo radial) can be generated with a toolbox [40]. Fig. 6 shows three different sampling schemes at a ratio of 33%. From the Table 1, we can see that our proposed method exhibits more accurate reconstructions with larger PSNR values than the other two methods for all sampling schemes. Fig. 7 shows the performance on test image Ortho1 employing 1D Cartesian sampling at a ratio of 33% using our proposed method and DLMRI. At the same time, Fig. 8 shows the performance on test image Ortho6 employing pseudo radial sampling at a ratio of 33%. The recovered images and the corresponding zoomed-in regions in Fig. 7 and Fig. 8 illustrate that our proposed method preserves the images structures and textures better than DLMRI and reproduces images with less errors. Fig. 9 shows the performance of the DLMRI and our proposed method on the Brain image employing 1D random Cartesian sampling of k-space with different sampling ratios. The sampling ratios in our simulation are 25%, 33% and 40%, respectively.

4.3. Performance with noise

To test the performance of our proposed method in the presence of a reasonable amount of noise, as the DLMRI does, zero-mean complex white Gaussian noise of standard deviation $\sigma = 18.8$ is also added in k-space. Fig. 10 shows the plots of PSNRs versus iteration number for DLMRI and our proposed method on the brain image with 33% 1D random Cartesian sampling, respectively. The larger PSNRs mean our proposed method is more robust to noise than DLMRI.

4.4. Performance with different dictionary learning algorithms

Because KSVD algorithm has fast convergence speed and the property of numerical stabilities relatively, we use KSVD for dictionary learning in our work. However, there are many other alternative dictionary learning algorithms, such as Method of optimal directions (MOD) [16], Online dictionary learning (ODL) [42], Block KSVD (BKSVD) [43], Incoherent KSVD (INK-SVD) [44] and Fast dictionary learning on classified patches (FDLCP) [45]. We use MOD, BKSVD and FDLCP as comparison algorithms in experiments. MOD uses a l_0 norm to measure signal sparsity, and applies the Least Mean Square Error Algorithm to update the dictionary. BKSVD belongs to structural dictionary learning algorithm, and it assumes that the signal can be represented jointly by a few subspaces. BKSVD attempts to find a dictionary that can perform block sparse representation of the signal and the block structure. To enhance the sparsity, FDLCP divides image into classified patches according to the same geometrical direction and dictionary is trained within each class. FDLCP combines the advantages of both reconstruction accuracy and reconstruction computation than the typical KSVD dictionary learning method.

Table 2 shows the performance on the Brain image, Ortho1 and Ortho6 under 2D Random sampling schemes at a ratio of 33% based on using different dictionary learning algorithms. In Table 2, KSVD, MOD, BKSVD and FDLCP represent reconstruction accuracies of the four dictionary learning algorithms respectively. KSVD + SADCT, MOD + SADCT, BKSVD + SADCT and FDLCP + SADCT represent reconstruction accuracies of the corresponding dictionary learning algorithm and our SADCT method under the SBI framework respectively. From Table 2, we can see that BKSVD and FDLCP show better reconstruction results than KSVD, because BKSVD and FDLCP make a development of KSVD from two aspects of dictionary structure and training sample distribution respectively. At the same time, we can also find that no matter what dictionary learning algorithm is, SADCT can always achieve more improvement. For KSVD, MOD, BKSVD and FDLCP, after adding DCT constraints to them, the reconstructed PSNR can increase 6.64%, 9.11%, 6.25% and 1.95% on average over the three test images, respectively. As the reconstruction accuracy of the dictionary learning algorithm is getting higher and higher, SADCT will slowly increase its rate of improvement. This shows that although SADCT is complementary to the above-mentioned dictionary learning algorithms, it has an upper limit of its representation ability as a sparse representation method.

4.5. Discussion on parameter settings

Compared to DLMRI, one more regularization term $\|\theta_w\|_{l_1}$ is introduced into our algorithm. Except for some parameters which are related to dictionary learning, such as the number of dictionary atoms K and patch size, the patch size used in SADCT and the adaptive scales h

are also discussed in this section. Each time, we set a varying parameter while keeping the rest parameters fixed to evaluate the sensitivity of our method. We also use the Brain image as the reference image, and the sampling scheme is 1D random Cartesian sampling at a ratio of 33%.

In Fig. 11(a) and (b), we discuss the number of dictionary atoms K and patch size. From the plots, we can see that along with K increasing, both the PSNR curves of DLMRI and our method have a rise. The reason is that the more atoms are learned from K-SVD, the finer those atoms can describe the image. We can also see that when the patch size is increased from 16 to 49, the PSNR values of DLMRI have a sharper decrease than our proposed method because of the weaker ability of large patch to depict a detail region. Our proposed method exhibits better robustness by combining with the SADCT, which can describe fine-scale image details effectively. In addition, we discuss the sparsity threshold for each patch T_0, patch overlap stride r. Fig. 11(c) shows the performance on the Brain image under 2D Random sampling schemes at a ratio of 33% using different sparsity thresholds. In Fig. 11(c), we can see that when the sparsity threshold is increased from 2 to 5, PSNR becomes larger. However, the PSNR performance degrades continuously after the sparsity threshold is increased from 5 to 7. The poorer performance at the low sparsity level such as 2 is due to the loss of resolution and higher sparse coding residuals occurring. When the sparsity is greater than 5, some atoms will bring redundant expressions, and aliasing artifacts will occur thereby degrading performance.

Patch overlap stride r indicates the degree of overlap of image patches, it not only affects the reconstruction accuracy but also the reconstruction speed. Table 3 shows the performance on the Brain image under 2D Random sampling schemes at a ratio of 33% using different patch overlap strides. In Table3, as the patch overlap stride increases from 1 to 4, PSNR descends. The patch overlap stride at the low level such as 1, which means there are more training samples and more patches that will participate in sparse reconstruction. On one hand, the richer the sample information, the stronger the expression ability of the trained dictionary. On the other hand, the higher the image patch overlaps, the stronger the ability to suppress noise. Based on the above analysis, we always select low patch overlap stride so that we can obtain higher reconstruction quality. However, from the Table 3, we can also see that due to more time will be consumed on sparse reconstruction, the decrease in patch overlap stride will increase computation cost.

In Fig. 12 we discuss the patch size used in SADCT and the adaptive scales h. There is a positive correlation between the patch size used in SADCT and the adaptive scales h, for example, if the patch size used in SADCT is 9×9, the adaptive scale h may be $\{1,2,3,4,5\}$. And if the patch size is 11×11, h may be $\{1,2,3,4,5,6\}$. Here, we just discuss the patch size used in SADCT, which is increased from 5×5 to 13×13 by a step of 2. The PSNR curves of our method with respect to different patch sizes used in SADCT are shown in Fig. 12. We can achieve a conclusion that the values of PSNR are slightly changed in general, which is because that different patch sizes have different abilities to depict detail regions. However, the property of adaptively recognizing the unknown smooth and anisotropic region in SADCT can slow down the difference of the abilities. In our simulation, we empirically set the patch size as 9×9, which plays the best performance relatively.

4.6. Algorithm convergence

Since the objective function of Eq. (4) is non-convex, it is difficult to give the theoretical proof for global convergence. Here, we only provide empirical evidence to illustrate the good convergence of the proposed algorithm. Fig. 13 shows the performance on the three test images employing 1D Cartesian sampling at a ratio of 33% using our proposed method. It is observed that with the growth of iteration number, all the PSNR curves increase monotonically and ultimately become flat and stable, which exhibiting good convergence property. Note that due to non-convexity of Eq. (4), it is natural that there are some perturbations in the curves.

5. Conclusion

In this paper, we proposed a novel method for the compressed sensing medical image recovery, which joints dictionary learning and Shape-Adaptive DCT (SADCT) thresholding. The dictionary trained by K-SVD is used to characterize the local sparsity that depicts the smoothness redundancies. At the same time, we use LPA-ICI to find the adaptive-shape region in the image patch. Then, SADCT is performed in that region to further exploit and enhance image sparsity. We employ the split Bregman iterations to solve the proposed optimization problem efficiently. The main contributions of this paper are in three ways. First, we propose to exploit sparsity of image in shape-adaptive regions, which is beneficial to medical images that always have a lot of complex textures. Second, as a new regularization term, SADCT can effectively alleviate the blurred structure information of the image resulting from the dictionary learning method of overlapping square patches. Third, based on split Bregman iterations, an efficient alternating minimization algorithm is developed to solve the proposed compressed sensing image recovery problem, which can achieve a fast and stable solution. Compared with RecPF and DLMRI, the results of numerical experiment demonstrate the effectiveness of the proposed method in terms of reconstruction accuracy. Many visual experimental examples indicate that the proposed method can produce sharp large-scale edges and fine-scale image details. The superior reconstruction performance of the proposed method means we can exploit sparsity in adaptive neighborhoods rather than square blocks. The proposed framework can also be extended to other image processing applications, such as denoising, inpainting and deblurring, etc.

Acknowledgment

This work is supported in part by the Major Projects of the National Natural Science Foundation of China under grant Nos. 41390450 and 41390454.

References

[1] Candes EJ, Romberg J, Tao T. Robust uncertainty principles: exact signal reconstruction from highly incomplete frequency information. IEEE Trans Inf Theory 2006;52(2):489–509.
[2] Donoho DL. Compressed sensing. IEEE Trans Inf Theory 2006;52(4):1289–306.
[3] Lustig M, Donoho DJ. Sparse MRI: the application of compressed sensing for rapid MR imaging. Magn Reson Med 1999;58(6):1182.
[4] Liang D, Liu B, Wang JJ, et al. Accelerating SENSE using compressed sensing. Magn Reson Med 2009;62(6):1574–84.
[5] Daubechies I, Defrise M, De Mol C. An iterative thresholding algorithm for linear inverse problems with a sparsity constraint. Commun Pure Appl Math 2004;57(11):1413–57.
[6] Beck A, Teboulle M. A fast iterative shrinkage-thresholding algorithm for linear inverse problems. SIAM J Imag Sci 2009;2(1):183–202.
[7] Bioucas-Dias JM, Figueiredo MAT. A new TwIST: two-step iterative shrinkage/thresholding algorithms for image restoration. IEEE Trans Image Process 2007;16(12):2992.
[8] Goldstein T, Osher S. The Split Bregman method for L1-regularized problems. SIAM J Imag Sci 2009;2(2):323–43.
[9] Yin W, Osher S, Goldfarb D, et al. Bregman iterative algorithms for L1-minimization with applications to compressed sensing. SIAM J Imag Sci 2008;1(1):143–68.
[10] Ravishankar S, Bresler Y. MR image reconstruction from highly undersampled k-space data by dictionary learning. IEEE Trans Med Imaging 2011;30(5):1028–41.
[11] Qu X, Guo D, Ning B, et al. Undersampled MRI reconstruction with patch-based directional wavelets. Magn Reson Imaging 2012;30(7):964.
[12] Candès EJ, Donoho DL. Ridgelets: a key to higher-dimensional intermittency? Philos Trans R Soc, B Sci 2000;357(1760):2495–509.
[13] Emmanuel JC, Donoho DL. Curvelets - a surprisingly effective nonadaptive representation for objects with edges. Astron Astrophys 2000;283(3):1051–7.
[14] Do MN, Vetterli M. The contourlet transform: an efficient directional multiresolution image representation. IEEE Trans Image Process 2005;14(12):2091–106.
[15] Lewicki MS, Sejnowski TJ. Learning overcomplete representations. Neural Comput 2000;12(2):337.
[16] Elad M, Aharon M. Image denoising via sparse and redundant representations over

learned dictionaries. IEEE Trans Image Process 2006;15(12):3736–45.
[17] Zhang J, Zhao C, Zhao D, et al. Image compressive sensing recovery using adaptively learned sparsifying basis via L0 minimization. Signal Process 2014;103(10):114–26.
[18] Aharon M, Elad M, Bruckstein A. K-SVD: an algorithm for designing overcomplete dictionaries for sparse representation. IEEE Trans Signal Process 2006;54(11):4311–22.
[19] Liu Q, Wang S, Ying L, et al. Adaptive dictionary learning in sparse gradient domain for image recovery. IEEE Trans Image Process 2013;22(12):4652–63.
[20] Zhan Z, Cai JF, Guo D, et al. Fast multi-class dictionaries learning with geometrical directions in MRI reconstruction. IEEE Trans Biomed Eng 2015;63(9):1850–61.
[21] Song Y, Zhu Z, Lu Y, et al. Reconstruction of magnetic resonance imaging by three-dimensional dual-dictionary learning. Magn Reson Med 2014;71(3):1285–98.
[22] Ma S, Yin W, Zhang Y, et al. An efficient algorithm for compressed MR imaging using total variation and wavelets. Computer Vision and Pattern Recognition, 2008. CVPR 2008. IEEE Conference on. IEEE. 2008. p. 1–8.
[23] Yang J, Zhang Y, Yin W. A fast alternating direction method for TVL1-L2 signal reconstruction from partial Fourier data. IEEE J Sel Top Sign Proces 2010;4(2):288–97.
[24] Sikora T. Low complexity shape-adaptive DCT for coding of arbitrarily shaped image segments. Signal Process Image Commun 1995;7(4–6):381–95.
[25] Sikora T, Makai B. Shape-adaptive DCT for generic coding of video. IEEE Trans Circuits Syst Video Technol 1995;5(1):59–62.
[26] Katkovnik V, Foi A, Egiazarian K, et al. Directional varying scale approximations for anisotropic signal processing. Signal Processing Conference, 2004, European. IEEE. 2004. p. 101–4.
[27] Katkovnik V. A new method for varying adaptive bandwidth selection. IEEE Trans Signal Process 1999;47(9):2567–71.
[28] Foi A, Paliy D, Katkovnik V, et al. Anisotropic Nonparametric Image Restoration Demobo. 2005.
[29] Koenen R. Overview of the MPEG-4 Standard, ISO/IEC JTC1/SC29/WG11 Doc. N3536. July 2000.
[30] MPEG-4. Information Technology - Coding of Audio-visual Objects - Part2: Visual, ISO/IEC 14496-2:2001. Dec. 2001.
[31] Foi A, Katkovnik V, Egiazarian K. Pointwise shape-adaptive DCT for high-quality denoising and deblocking of grayscale and color images. IEEE Trans Image Process 2007;16(5):1395–411.
[32] Venkataramani R, Bresler Y. Further results on spectrum blind sampling of 2D signals//International Conference on Image Processing, 1998. ICIP 98. International Conference on Image Processing, 1998. ICIP 98. Proceedings. IEEE. vol. 2. 1998. p. 752–6.
[33] Tropp JA. Greed is good: algorithmic results for sparse approximation. IEEE Trans Inf Theory 2004;50(10):2231–42.
[36] Eslahi N, Aghagolzadeh A. Compressive sensing image restoration using adaptive Curvelet thresholding and nonlocal sparse regularization. IEEE Trans Image Process 2016;25(7):3126–40.
[38] Yang J, Zhang Y. RecPF code Available http://www.caam.rice.edu/optimization/L1/RecPF/; 2010.
[39] Ravishankar S, et al. DLMRI code Available https://netfiles.uiuc.edu/ravisha3/www/DLMRICODE.zip; 2011.
[40] Lustig M, et al. sparseMRI_v0.2 toolbox Available http://www.stanford.edu/mlustig/; 2007.
[42] Mairal J, Bach F, Ponce J, Sapiro G. Online learning for matrix factorization and sparse coding. J Mach Learn Res 2010;11(1):19–60.
[43] Zelnik-Manor L, Rosenblum K, Eldar YC. Dictionary optimization for block-sparse representations. IEEE Trans Signal Process 2012;60(5):2386–95.
[44] Mailhe B, Barchiesi D, Plumbley MD. INK-SVD: learning incoherent dictionaries for sparse representations. Proceedings of the 2012 International Conference on Acoustics, Speech and Signal Processing. Kyoto, Japan: IEEE. 2012. p. 3573–6.
[45] Zhan Z, Cai JF, Guo D, et al. Fast multiclass dictionaries learning with geometrical directions in MRI reconstruction. IEEE Trans Biomed Eng 2016;63(9):1850–61.